JOURNAL OF AIRCRAFT
Vol. 41, No. 6, November–December 2004

Three-Dimensional Integrated Thermodynamic Simulation for Wing Anti-Icing System

Hugh H. T. Liu* and Jun Hua†
University of Toronto, Toronto, Ontario M3H 5T6, Canada

Thermal flow in an aircraft wing leading-edge anti-icing system is a complicated physical phenomenon and remains a challenging research topic of modeling and analysis. This paper presents a complete three-dimensional simulation of a wing segment including the piccolo-type thermal anti-icing bays inside the leading edge is presented. The Navier–Stokes analysis has been conducted for the integrated internal/external thermal flows with heat conductivity through the solid skin. The fully structured zones and boundary-layer meshing have reduced the total cell number and enhanced the near-wall impingement and the heat transfer analysis. Simulation results visually reveal the hot/cold flow interactions and heat conductivity through the fluid and solid zones. The calculated leading-edge surface temperature is compared with flight-test data of a similar configuration. The computational fluid dynamics model and its analysis under different flight conditions and configuration modifications provide a valuable assessment for wing anti-icing system research and development.

Nomenclature

E	=	energy, N · m
h	=	specific enthalpy, N · m/kg
h_{eff}	=	effective surface heat transfer coefficient N/m · s · K
M	=	Mach number
P, p	=	static pressure, Pa
P_0	=	total pressure, Pa
Re	=	Reynolds number
T	=	static temperature, K
T_0	=	total temperature, K
t	=	time, s
U	=	velocity, m/s
u_i, u_j, u_k	=	velocity components, m/s
x, y, z	=	Cartesian coordinates, m
α	=	angle of attack, deg
η	=	global thermal efficiency
ρ	=	density, kg/m^3
τ	=	share stress, N/m^2

I. Introduction

THE problem of aircraft in-flight icing remains severe threat to flight safety. For the past decade, research has been focusing on studies of aircraft icing caused by supercooled large drops (SLDs). Related topics include but are not limited to the following: 1) icing environment characterization and forecast, for example, recent Canadian research reported by Isaac et al.[1]; 2) ice accretion simulation using computational fluid dynamics (CFD) tools such as FENSAP-ICE-based simulation[2,3] and LEWICE3D-, ICEGRID3D-, and CMARC-based simulation[4]; and 3) better assessment and techniques in aircraft systems design to prevent icing or to remove ice. The last topic is of interest to the authors of this paper.

Aircraft wing leading edges are very vulnerable to ice accretion, due to their direct exposure to the oncoming flow and the largest local velocity and temperature gradients in the external flows. The most popular choice of ice prevention at the wing leading edge is a thermal anti-icing system. The hot air is bled from the engine compressor and ducted forward to a pipe with small holes known as a piccolo tube. The hot air jets from the small holes and then impinges on the inner surface of the leading-edge skin to keep the temperature of the outside surface above that of the icing condition. The surface temperature is controlled through regulating the hot airflow.

Recent thermal anti-icing investigations include both experimental and analytical approaches. From an experimental point of view, recent Canadian research on aircraft in-flight icing[1] has involved a large number of experimental flights in SLD areas since 1995. Brown et al.[5] conducted a correlation study with a segment model of a typical thermal anti-icing device in a wind tunnel. From an analytical perspective, Morency et al.[6] calculated the heat and mass transfer in the ice accretion process of the external flow over an electrically heated two-dimensional airfoil leading edge. Wang et al.[7] combined an adaptive response surface method (ARSM) optimization method with a potential flow solver and a heat conductivity code for solid materials to optimize the two-dimensional shape of a helicopter engine cooling bay surface. Perhaps the work most related to aircraft design was reported by de Mattos and Oliveira.[8] It presents a three-dimensional Navier–Stokes (NS) analysis with conjugate heat transfer of a wing-slat slice with a piccolo tube using a fully unstructured FLUENT code. It is an integrated slat slice external flow with the internal hot airflow, taking into account the wall conductivity of the slat skin. Surface temperature and thermal efficiency were discussed. Because of the consideration of computational efficiency, only the piccolo tube holes in one span section had been simulated. However, the external flowfields would have been more accurate if the main wing after the slat had been modeled.

In this paper, we present a numerical model to analyze and simulate the full three-dimensional integrated internal/external thermal flows of a complete wing segment with the anti-icing system. The wing model is developed using a modern CFD tool that includes the anti-icing piccolo tube in the bay and is such that the external flowfield could be more accurately simulated. Furthermore, a fully structured grid is also considered favorable for reducing the total grid cell numbers to improve the computational efficiency. Real skin conditions with heat transfer and conductivity are considered. Also investigated here are the three-dimensional wing leading-edge skin temperature distributions and the heat transfer efficiencies responding to the change in flight conditions, piccolo tube hot air inlet conditions, and the adjustments of the inlet and exhaust configurations to provide better knowledge of the thermal mechanism for the anti-icing system development. The major contributions of this paper, compared to the aforementioned research publications, are the simultaneous coupled solutions of the hot-air internal flow, the heat conductivity

Received 3 October 2003; revision received 11 February 2004; accepted for publication 12 February 2004.

*Assistant Professor, Institute for Aerospace Studies, 4925 Dufferin Street; liu@utias.utoronto.ca. Member AIAA.

†Research Fellow, Institute for Aerospace Studies, 4925 Dufferin Street.

through the solid skin, and the external flow of a complete wingspan segment.

II. Geometric Model

In a typical flowchart of a wing anti-icing system (WAIS), the hot air from the turboengine is introduced to the leading edge through a high-pressure valve and a wing anti-icing valve (WAIV). The control module regulates the WAIV to control the temperature of the leading-edge surface. Because the icing condition associated with SLDs can occur outside the certification environment,[1] and may be very difficult to test in wind tunnels or flights, a CFD model and analysis can serve as a valuable and cost-effective alternative to explore the WAIS behavior more safely or when detailed flight test data are not available at the preliminary design phase.

Figure 1 gives a geometry model of the present CFD simulation. The three-dimensional wingspan segment is composed from a supercritical airfoil NPU8, originally designed for a jet passenger aircraft.[9] The chord length of the wing is 1260 mm, and the thermal anti-icing system was inserted into the first 7% chord of the wing.

Figure 2 shows the details of the thermal devices in the leading-edge bay, which consists of 1) a piccolo tube on which there are a number of small holes to let the hot-air jets impinge the leading edge—the small holes are staggered in two rows of angles 15 deg up or down from the wing chord plane; 2) the leading-edge skin (not shown here) to be heated by the hot air in the anti-icing operation—the skin is chosen to be a 1.7-mm-thick aluminum sheet; 3) two exhaust holes on the lower side of the leading-edge skin to allow the hot air in the bay to exit to the external flow; 4) two ribs to separate the bays, with the hoses on the ribs neglected; and 5) the heat shield serving as the back wall of the bay model.

Fig. 1 A wingspan segment with the thermal anti-icing bay.

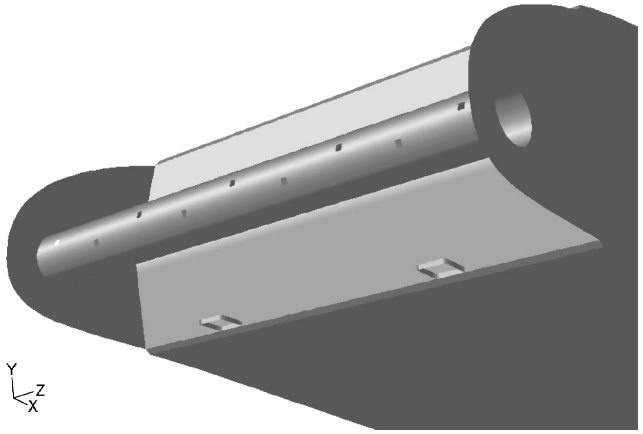

Fig. 2 Bay details with two exhaust holes (leading-edge skin not shown).

III. Numerical Thermodynamic Simulation

A. Navier–Stokes Solver

The CFD analysis method used in this research is the well-known NS solver FLUENT version 6.0. Its reliability has been demonstrated by a great number of aerospace and industrial applications.

In this method, conservation equations for mass and momentum, an equation for energy conservation, and additional transport equations for turbulent flows are solved with a finite volume approach over structured, unstructured, or hybrid grids. The method provides different solver formulations and several turbulence models.

For heat transfer, the following energy equation is solved in FLUENT:

$$\frac{\partial}{\partial t}(\rho E) + \frac{\partial}{\partial x_i}[u_i(\rho E + p)] = \frac{\partial}{\partial x_i}\left[k_{\text{eff}}\frac{\partial T}{\partial x_i} - \sum_{j'} h_{j'} J_{j'} + u_j(\tau_{ij})_{\text{eff}}\right] + S_h \tag{1}$$

where k_{eff} is the effective conductivity, $J_{j'}$ is the diffusion flux of species j', and S_h includes heat of chemical reaction and any other volumetric heat sources. To validate the pressure work, the kinetic energy and the viscous dissipation terms, the "enable-energy" and "viscous-heating" options are selected.

Attention is also paid to the heat transfer between the hot/cool flows and the skin surfaces. In this solver, the law of the wall for mean velocity yields

$$U^* = (1/\kappa)\,\ell_n(Ey^*) \tag{2}$$

where κ is the von Kármán constant and E is an empirical constant.

In the solid regions, like the skin with certain thickness, the following energy transport equation is used:

$$\frac{\partial}{\partial t}\rho h + \frac{\partial}{\partial x_i}(u_i \rho h) = \frac{\partial}{\partial x_i}\left(k\frac{\partial T}{\partial x_i}\right) + \dot{q}''' \tag{3}$$

where the last term in the right-hand side is the volumetric heat source.

Quantities also of interest in this simulation include the mass flow rate and the total heat transfer rate through the piccolo-tube injection holes and the total heat transfer rate through the skin surface to the external flows. The calculation of the surface heat transfer coefficient is based on the following equation:

$$h_{\text{eff}} = q''/(T_{\text{wall}} - T_{\text{ref}}) \tag{4}$$

where, q'' is the heat flux, T_{wall} is the wall temperature, and T_{ref} is the reference temperature taken as the static temperature of the oncoming flow.

The global thermal efficiency η is another measure of the effectiveness of a thermal anti-icing system, which is defined as the following:

$$\eta = (T_{\text{inlet}} - T_{\text{exhaust}})/(T_{\text{inlet}} - T_{\text{external}}) \tag{5}$$

The segregated scheme and Spalart–Allmaras turbulent model are applied in this integrated internal/external thermal flow simulation. This selection is based on the numerical experiment of applying different combinations of the solver schemes and turbulent models to internal and external flows separately. The calculated wing-section external flow results are compared with the wind-tunnel data of the NPU8 airfoil,[10] whereas the internal flows are verified by comparing the results of continuously refined mesh adaptation.

B. Mesh Generation

Unstructured grids are widely used in industry CFD applications and flows around complicated configurations. In the case of this anti-icing study, when computer memories and runover time become a concern for the complex three-dimensional coupled interior/exterior flows, when the accurate simulations of the viscosity, vortices, near-wall heat transfer, and conductivity are expected for

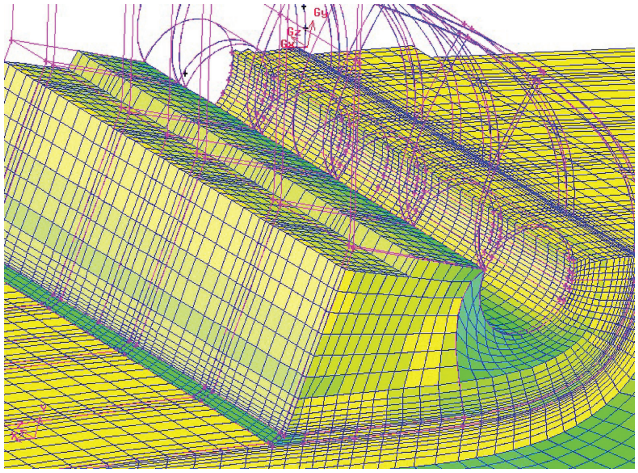

Fig. 3 Mesh near the wing leading edge.

a mesh with a lower cell number, and when the mesh is supposed to provide enough computation efficiency, the structured grid with fine near-wall resolutions would be a more favored choice. With the mesh generation tool GAMBIT, a structured grid for the complete internal/external flowfields is successfully generated for our wing anti-icing model.

For the wing external flow computations, a three-dimensional C-H mesh (C type mesh in chordwise and H type in spanwise) is used. The mesh features a boundary-layer grid near the wing surface and the refined mesh around the wing and the wake. The outer boundary is located five chord lengths away from the wing chord plan.

Figure 3 provides a closeup view of the grid near the leading edge. The interior grid also has a boundary-layer mesh and refinement near the impinging area. The interior and exterior meshes are connected through the mesh in the exhaust holes. Structured mesh is also used inside the aluminum skin for the heat conductivity calculation.

The grid of a half-model contains altogether 521,664 hexahedral cells. The number of cells is much less than that of an unstructured mesh of similar resolution.

A pressure far-field boundary condition (BC) is used for the external field. The pressure inlet BC is given at the piccolo tube holes. Symmetrical BCs are applied on the side faces of the external doming and the sidewalls of the solid skin. Wall BCs are specified for all the inner surfaces of the bay, the outer surface of the wing, and the bay ribs. Besides the lip skin, all the other surfaces were treated as adiabatic.

C. Analysis of the Three-Dimensional Simulation Results

For each simulation case, the far-field flight conditions and the inlet conditions at the piccolo tube holes are specified. The case 1 conditions are given as follows: far-field $M = 0.28$, $\alpha = 4.5$ deg, $T = 263$ K, and $P = 63{,}000$ Pa; the inlet conditions at the piccolo holes are $T_0 = 454$ K and $P_0 = 90{,}000$ Pa.

The computation takes a few hours on a Unix workstation for about 2000 iterations. The external flow, reported by the lift coefficient C_L, usually converges at 600 iterations, whereas the residuals converge to the given criteria at 1600 iterations.

Figure 4 presents a streamline plot over the wing surface, inside the bay, and on the symmetric plan of the half-span of the model. Colored by Mach number, the streamlines show the low-speed flow near the stagnation line and inside the bay; they also show the high-speed region over the upper surface of the wing and from the piccolo-tube holes. The streamlines of the exhaust air join the external flow and then turn downstream.

Figure 5 plots part of the streamlines inside the bay. It shows the higher impingement speed near the leading edge. The upper portion of the bay has three-dimensional circulated flow with more crossflows near the upper-rear corner of the bay. The crossflows move toward the span sections where the exhaust holes are located on the bottom of the bay.

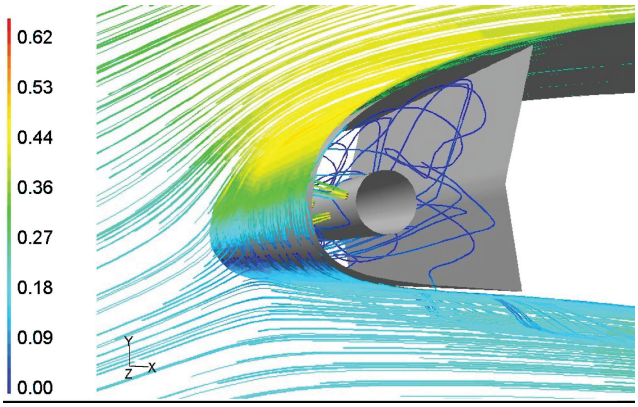

Fig. 4 Part of the streamlines of the flow (colored by Mach number).

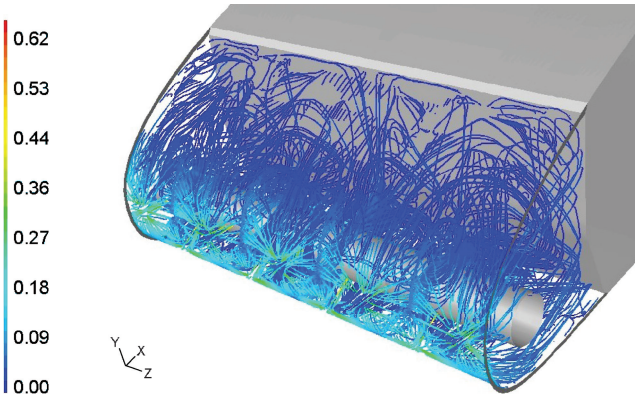

Fig. 5 Part of the streamlines of the internal flow (colored by Mach number).

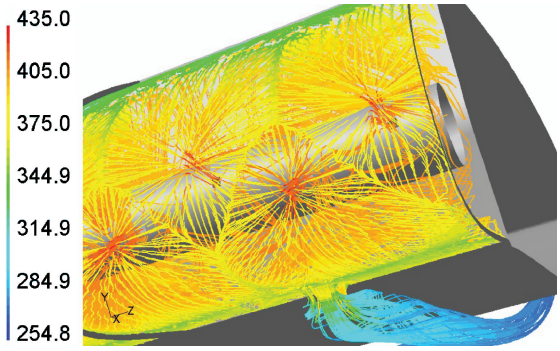

Fig. 6 Part of the internal flow streamlines (colored by static temperature, K).

Figure 6 also shows the inside streamlines, but colored by static temperature. The temperature is high at the area where hot-air jets impinge the inner skin surface; it decreases faster in the upper side than the lower side; and the air from the exhaust holes is still hot and then becomes cold while mixing with the external flows. The lower side internal flow is mostly chordwise before turning to the exhaust holes. The interaction lines between each impingement could also be identified.

For the anti-icing system under operation, the outside skin surface temperature distribution is one of the most expected quantities, which is shown in Fig. 7 for case 1. In the equilibrium among the inside heat transfer, the skin conductivity, and the outside heat transfer, the maximum temperature is around the leading edge where the hot air impinges on the bay. The temperature decreases continuously downstream in both upper and lower sides of the wing. The temperature contour on the sidewall reflects the comprehensive temperature changes inside the bay. It is noticed that

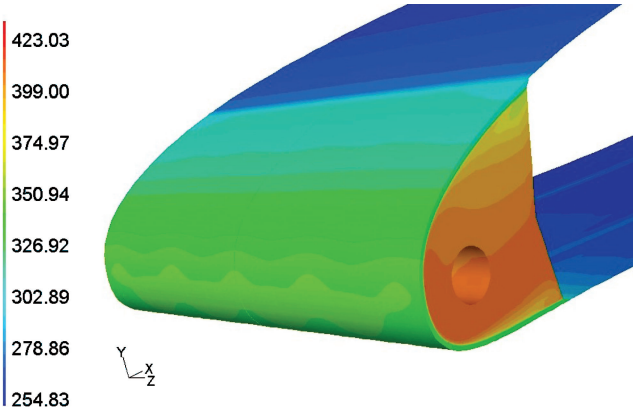

Fig. 7 Temperature distributions over the skin surface (K).

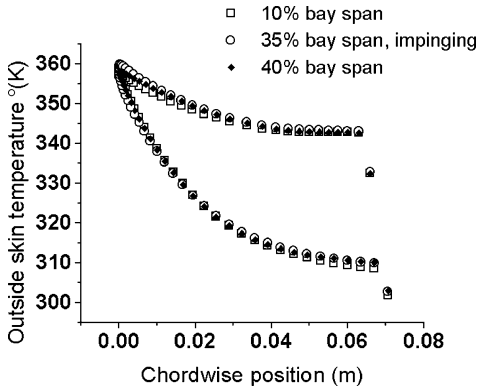

Fig. 8 Outside skin temperature along the chord of different bay sections.

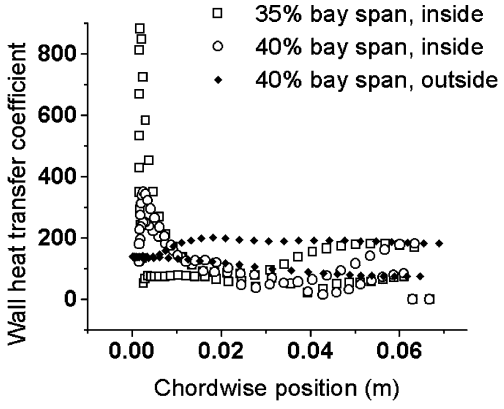

Fig. 9 Inside and outside surface heat transfer coefficient along the chord.

the rear-upper corner of the bay has less heat than the rest of the leading edge.

Figure 8 presents the leading-edge outside surface temperature distributions at different wingspan sections; the temperature values along the span are almost coincident. The maximum temperature occurs at the leading edge; the surface temperature over the upper side reduces faster than that over the lower side, as discussed before. The 35% bay span section has a piccolo-tube hole; therefore, the leading-edge temperature is slightly higher.

Figure 9 is the plot of heat transfer coefficient of both inside and outside skin surfaces in two span sections. The 35% bay span section has the impingement of the hot air at −15 deg, and so the coefficients are higher than that of the 40% bay span section, which is between two impingement sections. The outside coefficients at different span sections coincide, except near the exhaust holes. It could be seen that the wall heat transfer coefficient has higher values where the

Table 1 Boundary conditions of cases

Case	M	α, deg	T, K	P, Pa
3	0.28	6.5	263	63,000
4	0.33	4.5	263	63,000

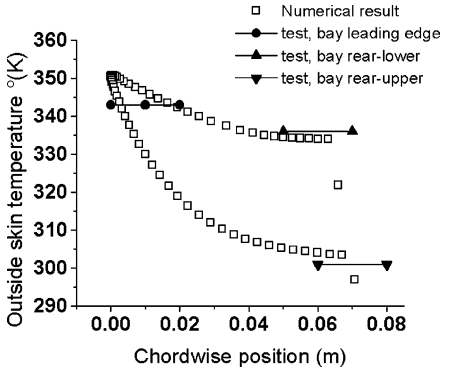

Fig. 10 Outside skin temperature compared with the test data of a similar WAIS.

flow speed is higher. This is mainly the contribution of the flux term in Eq. (4). The internal values seem to be higher also where more heat flux is needed from the outside, such as the upper surface and the rear ends of the bay, where the skin temperatures are lower; so does the $(T_{\text{wall}} - T_{\text{ref}})$ term in Eq. (4).

D. Comparison with Available Test Data

To evaluate the accuracy and feasibility of the present coupled thermodynamic analysis, numerical results are compared with flight measurements of a similar configuration. The comparison is done under the test case (case 2): far-field $M = 0.31$, $\alpha = 3.5$ deg, $T = 263$ K, and $P = 63{,}000$ Pa; the inlet conditions at the piccolo tube holes are $T_0 = 454$ K and $P_0 = 87{,}500$ Pa.

Because the present model is different from the test wing in airfoil coordinates, piccolo-tube locations, and other geometry details, comparisons are limited to the skin temperature ranges, as shown in Fig. 10. The measured data are plotted over a certain chord region because the actual locations of the temperature sensors over the leading edge are not specified.

The comparison shows that the numerical results are within the test data range for both upper and lower surfaces and are close at the nose of the wing. This result suggests that the present CFD simulation is reasonable, and this CFD modeling approach could be used as an alternative tool for the research and development of the wing anti-icing system.

IV. Thermodynamic Analysis for the Wing Anti-Icing System Development

The second part of the CFD three-dimensional simulation is to investigate the capability of design assessment in the process of the WAIS development. Our investigations include the analysis in response to the changes of flight conditions, piccolo-tube inlet heat fluxes, and configuration modifications.

A. Temperature Recovery for the Change of Flight Conditions

First investigated is the effect on the wing surface temperature distributions due to the change of flight Mach number and angle of attack, as labeled in two new cases (cases 3 and 4) in Table 1.

Figure 11 plots the leading-edge external surface temperature distributions of the 40% span section for flight-condition changes around the base case, case 1 ($M = 0.28$, $\alpha = 4.5$ deg), while Fig. 12 shows the corresponding plots of the outside surface heat transfer coefficient (SHTC).

Increasing α from 4.5 deg (case 1) to 6.5 deg (case 3) causes the surface temperature to decrease 2 K on the lower surface and 3–4 K over the upper side. The heavier drop of the upper surface

Table 2 Change of the inlet boundary conditions

Case	Inlet T_0, K	Inlet P_0, Pa
5	458	92,500
6	453	92,500
7	458	90,000

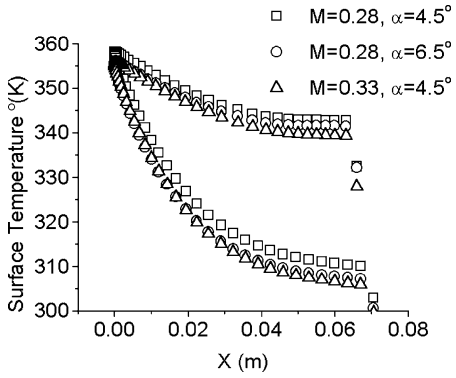

Fig. 11 Chordwise outside skin temperature for different flight conditions.

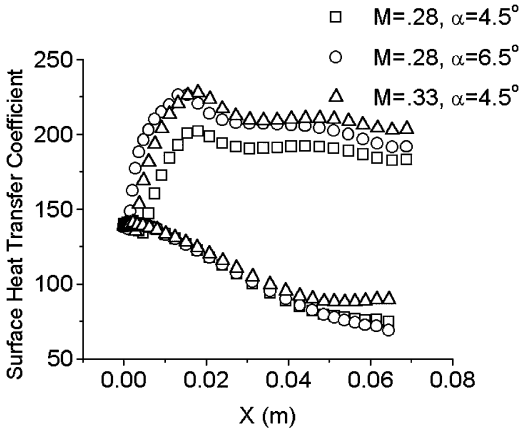

Fig. 12 Chordwise outside skin heat transfer coefficient for different flight conditions.

temperature is due to the corresponding increase of the external velocity over the upper surface. As shown in Fig. 12, the SHTC values on the lower surface remain almost the same as in case 1, but the values over the upper surface jump sharply, especially near the nose where the surface velocity reaches the maximum. This suggests that the angle of attack changes the profile of the SHTC curve.

Increasing Mach number from 0.28 (case 1) to 0.33 (case 4) would decrease the external surface temperature by 3 K near the nose and 5 K near the end of the heated bay due to the additional heat transfer to the faster external flows. It is interesting to notice that the SHTC values for the upper surface increase almost a similar amount, reflecting the overall flow acceleration due to the increase of Mach number.

To recover the surface temperature level, that is, from the case 3 temperature back to the case 1 values, the heat flux from the piccolo tube is increased either by increasing inlet total temperature and pressure together or by increasing them separately. (The external flow conditions are the same as those in case 3.) Three new cases are designed in Table 2.

Figure 13 gives the corresponding surface temperature plots. The case 1 and 3 results are also plotted for reference. It could be seen that 1) the case 5 inlet condition has increment in both T_0 and P_0—it brings the surface temperature almost back to the case 1 values—but it has a little overheating on the lower side and some underheating on the upper side of the leading edge; and 2) cases 6 and 7 change

Table 3 Fluxes and the global thermal efficiency

Case	Inlet MFR, kg/s	Inlet THTR, W	OSTHTR, W	η
1	0.00299	466	158	0.139
3	0.00297	464	162	0.157
5	0.00311	500	168	0.135

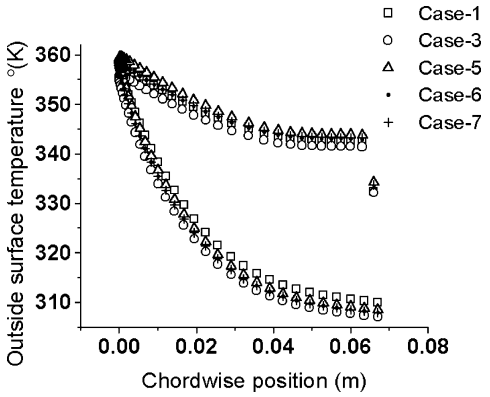

Fig. 13 Outside skin temperature for different piccolo inlet conditions.

either T_0 or P_0 alone—the temperature increments are both almost half that of case 5, suggesting that changing either T_0 or P_0 for a similar heat flux increment would lead to a similar amount of surface temperature change.

The corresponding changes of fluxes and the global thermal efficiency are shown in Table 3. Comparisons are given of the inlet mass flow rate (MFR) and inlet total heat transfer rate (THTR) through all the small holes on the piccolo tube. The outside skin surface total heat transfer rate (OSTHTR) and the global thermal efficiency η are also compared.

The increase of α in case 3 from case 1 raised the exhaust pressure at the lower surface exhaust holes; the inlet heat flux was then reduced slightly. Meanwhile, more heat was brought away by the external flows as the upper surface velocity increased.

With the increase of inlet T_0 and P_0 in case 5, both MFR and heat transfer rate from the piccolo-tube holes increased accordingly, and the outside surface heat exchange increased too, accompanied by the surface temperature recovery.

The global thermal efficiency, calculated by the average static temperature values at the piccolo-tube injection holes and bay exhaust holes, as well as the far-field static temperature provides a similar analysis result. Global thermal efficiency increases when more heat is transferred to the external flows through the skin, but not necessarily reflecting the skin temperature levels.

B. Temperature Improvement with Configuration Modifications

In general, the chordwise surface temperature profile has higher values on the lower surface than over the upper surface. This profile would normally suit the common ice accretion shapes with more ice over the lower side.[11] But there are also situations like the reicing of the runback water or ice remaining on the rear-upper bay or aft of the heated leading edge.[1] On the other hand, there exists the risk of overheating at the nose if more heat flux is simply added through the piccolo tube to make the rear-upper bay hotter. In these circumstances, it is necessary to improve the temperature profiles to provide more heat transfer over the upper surface without increasing the piccolo-tube heat flux. Modifying the bay configurations to change the surface temperature distribution via the change of the internal flow patterns could be an alternative choice. The following presents our investigation using the CFD tools.

The first attempt is to change the hot-air injection angle from the piccolo tube. One row of the holes is moved to the same line of the other row so that the injection angles are either all $+15$ deg or all -15 deg, instead of half/half as in the original configuration. The inlet and far-field conditions are kept the same as in case 1.

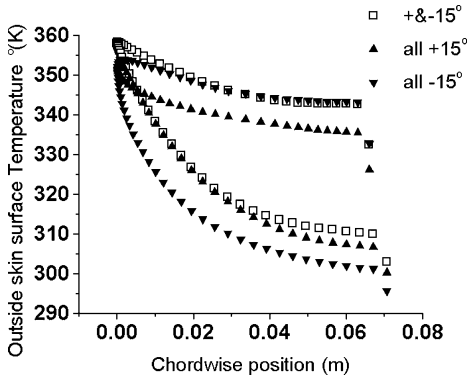

Fig. 14 Outside skin temperature of different piccolo-tube injection angles.

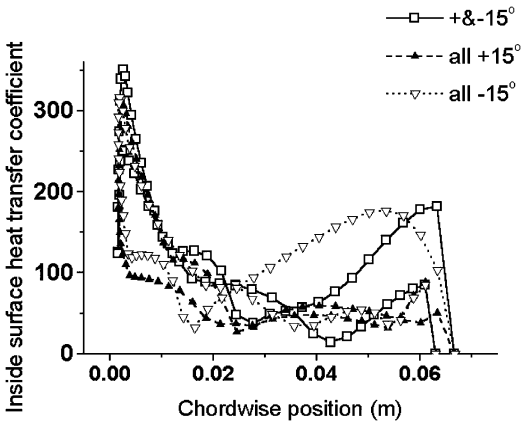

Fig. 15 Chordwise heat transfer coefficients of different piccolo-tube injection angles.

Simulation results are plotted in Fig. 14, together with those of case 1 for reference.

The +15 deg injection case reduces the lower surface temperature, whereas the −15 deg model reduces the upper surface temperature. Neither of them could increase the temperature of their own side. Meanwhile, the nose temperature values decreased in both cases.

The reason is considered to be the reduction of total effective impingement area of the hot-air jets on the inner surface when the two-row-staggered holes are relocated into one un-staggered row. Therefore, the results of these two cases suggest that 1) changing the injection directions could change the skin surface temperature profile and 2) the reduction of the total effective impingement area of the hot air on the inner surface will reduce the total heat transfer from the hot air to the skin and result in a temperature decrease over the outside surface.

The preceding analysis is further supported by the profile of the inside surface heat transfer coefficient as shown in Fig. 15. The curve corresponding to the original two row injections has two peaks near the nose, indicating higher heat transfer rates and larger effective impingement area, whereas either + 15 or −15 deg cases have only one peak, indicating the reduction of heat transfer.

The second attempt is to bring the exhaust holes from the lower skin to the back shield near the upper-rear corner of the bay to bring more heat to the upper side. Figure 16 shows the configuration colored by the computed temperature contours. The inlet and far-field conditions are the same as those in case 1 and a pressure outlet condition is given at the exhaust holes, where P and T are set to be the same values at the exhaust holes of the case 1 flow.

Figure 17 plots the outside surface temperature distributions on a 40% bay span section for both original and new exhaust locations. The upper surface temperature is effectively increased while the lower side decreased. This example suggests that changing the exhaust hole locations could improve the skin temperature profile.

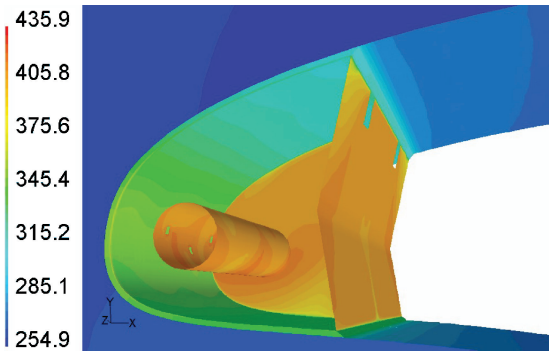

Fig. 16 Temperature contours of top located exhaust holes (K).

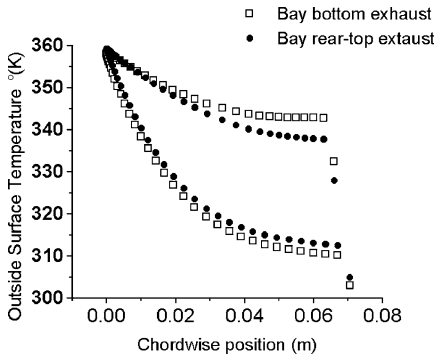

Fig. 17 Outside skin temperature distributions for different exhaust hole locations.

C. Findings and Observations

The surface temperature could be recovered by the adjustment of the piccolo-tube heat flux in the correct amount, but overshoot and undershoot may occur for upper or lower sides of the leading edge.

The change of the hot-air injection directions inside the bay could change the outside surface temperatures but may not improve the temperature distribution profile.

The total effective impingement area of the hot air over the inner surface has significant impact on the total heat transfer rate and then the outside skin temperature.

The relocation of the exhaust holes could improve the external temperature profile via the modification of the internal flow pattern and heat transportation.

V. Conclusions

This paper summarizes the major results of a complete three-dimensional wing segment model development with the piccolo-type thermal anti-icing bays inside the leading edge, and the integrated internal/external thermal flow simulation with heat conductivity through the solid skin, using the NS solver FLUENT software. To improve computational efficiency, the CFD analysis features a full structured mesh for the flow, impingement, and heat transfer simulations.

The simulation results have shown detailed thermal fluid quantities of the interacted hot/cold flows and the heat fluxes and have provided comprehensive knowledge of the phenomenon. The calculated outside surface temperature distributions are within the range of the flight-test data of a similar configuration.

The investigations with this CFD model for different flight conditions, piccolo-tube inlet heat flux conditions, and configuration modifications also provide valuable observations for the development of the WAIS.

Acknowledgments

The research work is supported by the Ontario Research and Development Challenge Fund and a research grant of the Natural Science and Engineering Council of Canada. The authors would like to

express their appreciation to Marius Paraschivoiu for providing access to the FLUENT CFD software. The work presented in this paper is also motivated by research collaboration between the University of Toronto Institute for Aerospace Studies (UTIAS) and Bombardier Aerospace (BA). The authors appreciated BA for providing access to some of their documents and data. Finally, the authors thank the anonymous reviewers for their valuable comments and suggestions.

References

[1]Isaac, G. A., Cober, S. G., Strapp, J. W., Korolev, A. V., Tremblay, A., and Marcotte, D. L., "Recent Canadian Research on Aircraft In-Flight Icing," *Canadian Aeronautics and Space Journal*, Vol. 47, No. 3, 2001, pp. 213–221.

[2]Bourgault, Y., Boutanios, Z., and Habashi, W. G., "Three-Dimensional Eulerian Approach to Droplet Impingement Simulation Using FENSAP-ICE, Part 1: Model, Algorithm, and Validation," *Journal of Aircraft*, Vol. 37, No. 1, 2000, pp. 95–103.

[3]Beaugendre, H., Morency, F., and Habashi, W. G., "FENSAP-ICE's Three-Dimensional In-Flight Ice Accretion Module: ICE3D," *Journal of Aircraft*, Vol. 40, No. 2, 2003, pp. 239–247.

[4]Bidwell, C. S., Pinella, D., and Garrison, P., "Ice Accretion Calculations for a Commercial Transport Using the LEWICE3D, ICEGRID3D and CMARC Programs," NASA/TM-1999-208895, 1999.

[5]Brown, J. M., Raghunathan, S., and Watterson, J. K., "Heat Transfer Correlation for Anti-Icing System," *Journal of Aircraft*, Vol. 40, No. 1, 2003, pp. 65–70.

[6]Morency, F., Tezok, F., and Paraschivoiu, I., "Heat and Mass Transfer in the Case of Anti-Icing System Simulation," *Journal of Aircraft*, Vol. 37, No. 2, 2000, pp. 245–252.

[7]Wang, D., Naterer, G. F., and Wang, G., "Thermofluid Optimization of a Heated Helicopter Engine Cooling-Bay Surface," *Canadian Aeronautics and Space Journal*, Vol. 49, No. 2, 2003, pp. 73–86.

[8]de Mattos, B. S., and Oliveira, G. L., "Three-Dimensional Thermal Coupled Analysis of a Wing Slice Slat with a Piccolo Tube," AIAA Paper 2000-3921, Aug. 2000.

[9]Hua, J., and Zhang, Z. Y., "Transonic Wing Design for Transport Aircraft," ICAS-90-3.7.4, Sept. 1990.

[10]Hua, J., Kong, F. M., Wang, J. J., Zhan, H., Sun, R. Z., Qiu, D., Fu, D. W., Liu, J. C., and Zhang, Z. Y., "Recent Examples on Design Aerodynamics for Transport Aircraft," ICAS-2002-2.5.2, Sept. 2002.

[11]Reehorst, A., Chung, J., Potapczuk, M., Choo, Y., Wright, W., and Langhals, T., "An Experimental and Numerical Study of Icing Effects on the Performance and Controllability of a Twin Engine Aircraft," NASA TM-1999-208896, 1999.